An automated segmentation for direct assessment of adipose tissue distribution from thoracic and abdominal Dixon-technique MR images

Jason E. Hill[a], Maria Fernandez-del-Valle[b], Ryan Hayden[a], Sunanda Mitra[a]*

[a] Dept. of Electrical and Computer Engineering, Texas Tech University, Box 43102
Lubbock, TX USA 79409-3102

[b] Dept. of Applied Health (Exercise Physiology), Southern Illinois University Edwardsville, Campus Box 1126, Edwardsville, IL USA 62026-1126

ABSTRACT

Magnetic Resonance Imaging (MRI) and Magnetic Resonance Spectroscopy (MRS) together have become the gold standard in the precise quantification of body fat. The study of the quantification of fat in the human body has matured in recent years from a simplistic interest in the whole-body fat content to detailing regional fat distributions. The realization that body-fat, or adipose tissue (AT) is far from being a mere aggregate mass or deposit but a biologically active organ in and of itself, may play a role in the association between obesity and the various pathologies that are the biggest health issues of our time. Furthermore, a major bottleneck in most medical image assessments of adipose tissue content and distribution is the lack of automated image analysis. This motivated us to develop a proper and at least partially automated methodology to accurately and reproducibly determine both body fat content and distribution in the human body, which is to be applied to cross-sectional and longitudinal studies. The AT considered here is located beneath the skin (subcutaneous) as well as around the internal organs and between muscles (visceral and inter-muscular). There are also special fat depots on and around the heart (pericardial) as well as around the aorta (peri-aortic). Our methods focus on measuring and classifying these various AT deposits in the human body in an intervention study that involves the acquisition of thoracic and abdominal MR images via a Dixon technique.

Keywords: Segmentation, Magnetic resonance images; Dixon technique; body fat content and distribution; adipose tissue; visceral adipose tissue; cardiac adipose tissue.

1. INTRODUCTION

Quantification of fat distributions has been carried out by various medical imaging modalities[2], and while Computed Tomography (CT) can yield a higher localized spatial resolution, due to concerns about ionizing radiation from CT, MRI is the preferred modality for general use in whole-body adipose tissue (AT) assessments. AT shows up as the brightest tissue (ignoring blood flow effects) in normal subjects when imaged by Inversion Recovery (IR) and the more robust T1-weighted (T1-w) MRI. Improved imaging technology as well as analysis techniques have led to various AT assessment approaches (see e.g. Tab. 1 in Ref. [1] and Tab. 3 in Ref. [3]), even allowing for the direct measurement of the whole-body fat distribution[4,5].

These developments have led to MRI and MRS being deemed as the gold-standard for assessing total fat content as well as regional distributions in the body[1]. First, semi-automated and later more fully automated segmentation of subcutaneous adipose tissue (SAT) and the visceral adipose tissue (VAT) for T1-w MRI volumes were carried out[6-9]. One issue faced by these approaches is the determination of multiple thresholds, which may require supervision[7]. Even the fully automated approach requires much prior geometric knowledge of the tissue distributions and models of the vertebrae column[8]. The use of the multi-echo Dixon technique along with a breath-hold is becoming more popular since it produces separately fat and water only images, simplifying the segmentation process, see e.g. Fig. 6.

Our work aims to automatically segment, identify and quantify various ATs from thorax and abdomen volumes acquired by magnetic resonance imaging (MRI) through a modified Dixon technique[1,3] with some guidance from annotated features. The scans, which were acquired with the purpose of evaluating exercise and dietary interventions in obese

---

*sunanda.mitra@ttu.edu; phone 1 806 834-8074 x 242; fax 1 806 742-1245

subjects[10,11], have been rectified and various anatomical landmarks have been annotated. Each subject underwent a multi-echo Dixon scan taken in two positions, one with the body coil over the thorax and upper abdomen, and the other more inferior covering the middle and lower abdomen, yet overlapping. Raw data from these Dixon scans comes in the form of four image volumes simultaneously acquired: (1) in-phase (IP) and (2) out-of-phase (OOP) image volumes, which are in turn used to calculate, on the machine with a proprietary algorithm, pairs of (3) fat-only and (4) water-only signal images. Since the fat-only and water-only image pairs are already aligned and co-registered they can be used as the basis for further segmentation of tissues. The goal is to compare the AT depots at pre-intervention and post-intervention to be used in conjunction with other biomarkers to infer the effect of these biologically active regions on human health and how to optimize health outcomes for the over-weight and obese.

What sets our work apart is that we attempt to not only segment the SAT and VAT with data acquired from the Dixon technique with automatic thresholding but we also classify the various fat depots around the heart as well, in the absence of cardiac gating. While it is expected that the absolute value of the heart fat from our segmentation needs to be calibrated due to motion blur induced by the heart beating, this segmentation method could be useful to quantify relative changes in heart fat depots in longitudinal or intervention studies, which is our target application.

2. METHODOLOGY

Here we report the preliminary analysis methodology of the pre-intervention and post-intervention MRI scans of 4 female subjects [18–30 years old with body mass index (BMI) = 30–40 kg/m^2]. The 3D MRI volumes of thorax and abdomen were processed in three steps: (1) rectification of the two volumes acquired by two separate body coils; (2) the labelling of anatomical landmarks for pre-/post-interventional comparison; (3) a progressive automatic segmentation of various tissue types. This post-processing and analysis were carried out in MATLAB R2016a (MathWorks Inc., Natick, MA, USA) with in-house scripts designed and written by the first author.

2.1 Study Design

All subjects completed a medical history screening, were established as healthy and required to maintain adequate compliance with the study requirements. Subjects were excluded if they had one or more of six characteristics: (1) being at high risk for cardiopulmonary events; (2) pregnant; (3) taking medications that affect endocrine or cardiovascular function; (4) having high blood pressure (i.e. systolic greater than 140 mmHg or diastolic greater that 90 mmHg); (5) engaging in low intensity strength training more than twice a week or moderate-high intensity training of any type and frequency; (6) having smoked tobacco products. Subjects were discontinued from the study if they failed to maintain adequate compliance of the study sessions or cooperation with the researchers during the visits, or no longer meet the inclusion criteria. The exercise intervention consisted of supervised circuit training in three sessions per week, each of which lasted about 45-50 minutes after a dynamic warm-up. The circuit included seven strength exercises engaging the major muscle groups. The participants performed three sets of ten repetitions, with resting periods of 30 seconds between exercises, and two minutes between sets. The intensity was set at 70-80% of one repetition maximum (RM). The load was changed depending on the participants' perception when needed based on the Adult OMNI Perceived Exertion Scale for Resistance Exercise (OMNI-RES) perception scale[12].

2.2 MRI Scan Protocol

For the MRI scanning process, the subjects lay in a supine, head first position with arms extended above their head (except in one scan); with a triangular support pillow under the knees. Two body coils were laid length-wise over the thoracic and abdominal regions with a small overlap prior to scanning. The two scans were successively acquired using a 3.0 T Skyra MRI system (Siemens, Munich, Germany) at the Texas Tech Neuroimaging Institute (TTNI), each taken with a 20-s breath-hold. Each scan involved the acquisition of 120, 2.5 mm thick axial images with a 20% gap (hence a separation of 3.0 mm between slice centers and a total extent of 36 cm), with a matrix = 320×260 of square voxels (widest FOV = 450 mm), yielding an effective voxel size of $1.40625 \times 1.40625 \times 3.0$ mm^3 (except for two scans that required larger FOVs). Imaging was performed using a multi-echo T1-weighted volumetric GRE sequence known as the Volumetric Interpolated Breath-hold Examination (VIBE) Dixon sequence [TR/TE = 3.97/1.23 ms, flip angle (FA) = 9°] along with the default factory settings[13,14]. This sequence is a multi-echo sequence that produces in-phase (IP) and out-of-phase image volumes; from these the Siemen's software reconstructs the fat-only and water-only signals as distinguished by their chemical shift, $\delta \sim 3$ ppm. It should be noted that the built-in phase unwrapping algorithm is
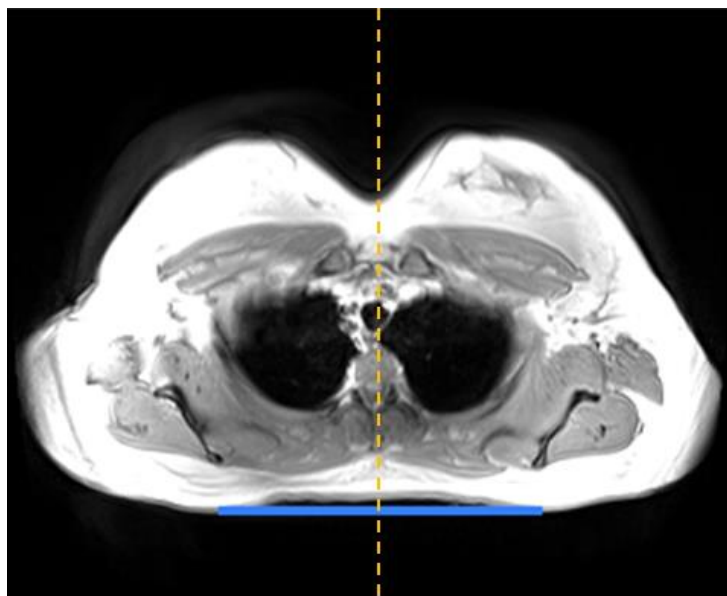
Figure 1. From a foreground thresholded image the most posterior points on right and left sides are found and used to construct a connecting line (blue) estimating the intersection line of the patient table plane with this slice plane. Then the coordinates of the intersection point between the table and the vertical line of bilateral symmetry that passes through the center of mass of the image is recorded allowing for the angles of the table plane to be estimated. The two larger voids are the lungs, and the smaller central void is the esophagus.

imperfect, and particularly near larger inhomogeneities (e.g. at the peripheries of the image) these phase unwrapping errors can cause some signals to be swapped between their proper designation as arising from fat or water.

2.3 MRI Volume Rectification

Rectification was guided by the MR scanner coordinates for each scan stored in the DICOM headers. The flat plane of the patient table was approximately determined from geometry, since the posterior contact points can be tracked across the slices and the pitch and role tilt angles estimated. First, the data from both fat and water signals are combined through a background threshold into an image that represents the main mass of the body. Next, the most posterior points on both right and left sides as well as the bilateral symmetry line of the body are found. Then, the approximate line of the patient table is constructed between the two posterior points and the intersection point of the table and the bilateral symmetry line is taken as the center-of-mass contact point with the table, see Fig. 1. The center-of-mass points of contact are then tracked slice by slice across a certain range (as determined by a calibration technique) in order to estimate the pitch tilt angle of the scan relative to the flat table in the direction of the MRI bore (Z direction), see Fig 2. The average roll tilt angle can also be tracked in a similar way by tracking the slope of the horizontal table line slice by slice. Yaw and roll angles are typically small or negligible if the body coils are perfectly aligned. After the tilt angles are found, the
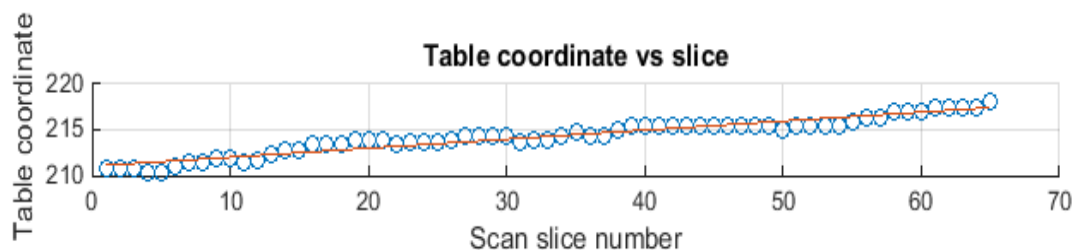

Figure 2. The plot of the center of mass contact point with the patient table vs. slice estimates a pitch tilt angle of 3.1559° from a linear regression for slices 1-65 of the superior thorax-including scan, from the same subject as in Fig. 1.

raw data volumes are rotated accordingly to achieve a flat table plane. Finally, the center of masses of the set of overlapping slices is used to properly align and combine the two volumes.

The center of masses of the set of overlapping slices is used to properly align and combine the two volumes. The resulting overlapping slices of the two scans still do not match up perfectly due to non-linear distortions in imaging near the edge of the body coil, so their segmentation results will be averaged, weighted by their distance from the edge to the first non-overlapping slice. In this way, the segmentation results of the two volumes can be seamlessly "stitched" together providing an integrated volume to use for comparison in longitudinal studies.

2.4 Labelling of Key Anatomical Landmarks

Next, several key anatomically associated points and axial slices were labelled for each rectified volume[15]. These include the center points of the aorta in the superior thorax-containing scan, as well as the slices containing the lowest fully thoracic slice (the diaphragm begins to appear in the next slice down), the apex of the heart, the middle of key intervertebral disks (L5-S1, L4-L5, L3-L4, L2-L3, L1-L2, T9-T10, T5-T6,that show up brighter in the water-only signal), the umbilicus, and the largest cross-section of the ball-like femoral heads. Based upon the shape of the lungs and the apex of the heart, the next lower intervertebral disk (typically around T9-T10) is taken to delineate the separation of the thorax from the abdomen, and the slice containing the widest cross-section of the femoral heads is used to estimate the abdominal floor location. Labelling these features is a laborious task, yet they guide the hereafter automatic segmentation process, and allow for a consistent comparison of pre- and post-intervention sessions, see Fig. 3.

2.5 Automated Segmentation

Similar to existing approaches[8-11], the slice-by-slice automated segmentation of the various ATs is carried out in stages via morphological and other image processing operations from the enhanced fat- and water-only signal foregrounds using the expected distribution of the various adipose tissues and organs. A 3D volume of each segmentation result is also constructed slice-by-slice, which sometimes aids in the segmentation of the next slice in the sequence; see e.g. Figs. 3(b) and 11.

2.5.1 Inhomogeneity correction

One issue with the raw signal data is that the peripheries tend to exhibit drop-off in signal intensity, see Fig 4(a). A preliminary contrast enhancement is first carried out with a sampling mask based on the expected location of the body
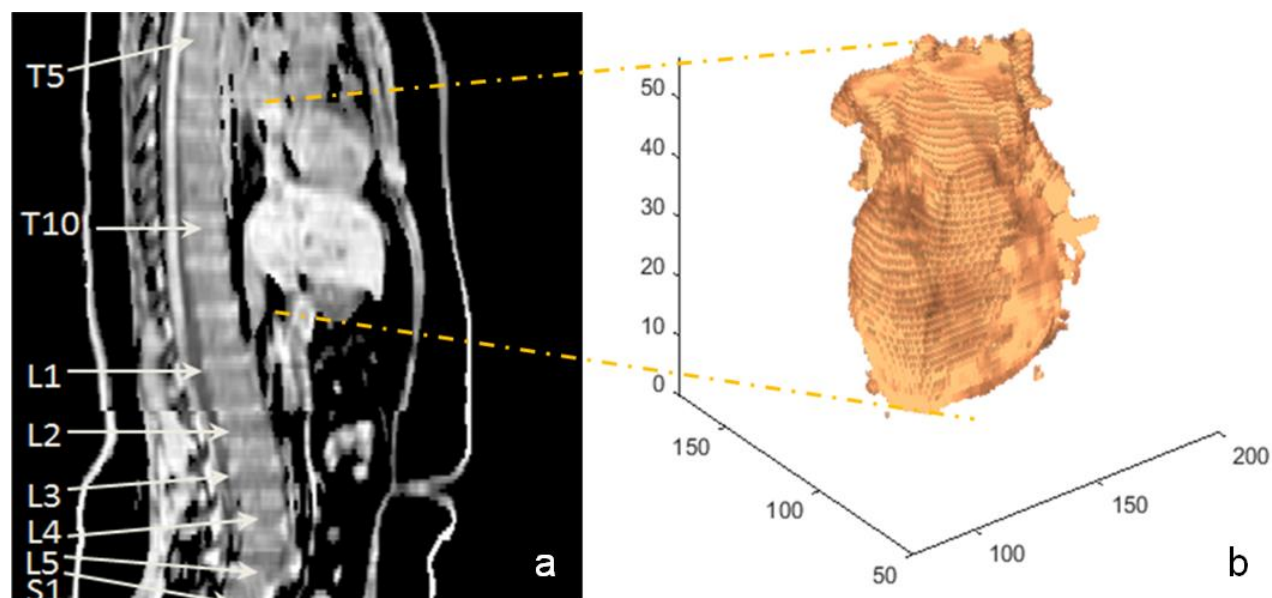

Figure 3. (a) The sagittal slice of the water-only signal derived from the Dixon-technique scan with some key vertebrae labeled. Note that the bright intra-vertebral disks serve as useful landmarks. (b) a 3D reconstruction of the heart organ tissue from the subsequent segmentation.

Figure 4. (a) The raw data of the water only signal (axial slice in abdomen around kidney area for subject B); the bright circle is the aorta. (b) Contrast enhancement derived from sampling the body cavity mask, not including center region to avoid the aorta. (c) Resulting normalized image after inhomogeneity correction, masking out of the background and contrast enhancement, which shows regions where the water-only signal is dominant.

cavity, which also avoiding sites of higher signal intensity, e.g. the aorta. Inhomogeneities are then suppressed in the data with the use of morphological closure with a large radius. See Fig. 4 for an example of this necessary procedure which yields an improvement in both segmentation and the estimation of fat and water fractions.

2.5.2 Histogram guided contrast enhancement

Next the non-background peak of a median filtered histogram is used for contrast enhancement, while the valley below the said peak is taken to be the threshold for foreground and background signals (all screened with Otsu's method[16] to avoid the over influence of outliers), see Fig. 5. In this way the foregrounds of the fat-only and water-only images are detected. This technique has been found to be robust over all subjects. The automatically determined threshold used to define the foreground is also used to generate normalized fat-only and water-only images, as well as fat and water dominant signal binary masks, which are taken as the preliminary segmentation of primarily water and fat bearing voxels, subject to later corrections, see Figs. 4(c), 5(b), and 5(c). Our automated segmentation in-house script then uses these normalized, enhanced images and these histogram-derived thresholds as the bases of further analysis.

2.5.3 Define void signal

In addition to the enhanced fat-only and water-only signals, it is also useful to construct a normalized "void" signal (see Fig.6) for a slice or ROI, which is defined as,

$$S_{\text{void}} = 2 - S_{\text{fat}} - S_{\text{water}}, \tag{1}$$

Figure 5. (a) The histogram of the inhomogeneity corrected fat-only abdominal image (subject B) with low-intensity background bins removed and relevant peak and valley pointed out. (b) Resulting contrast enhanced image, where the peak is taken as maximum intensity, and (c) the adjusted valley intensity value is used as an automatically determined threshold to segment the foreground fat signal from everything else, resulting in a binary mask for all types of adipose tissue (AT).
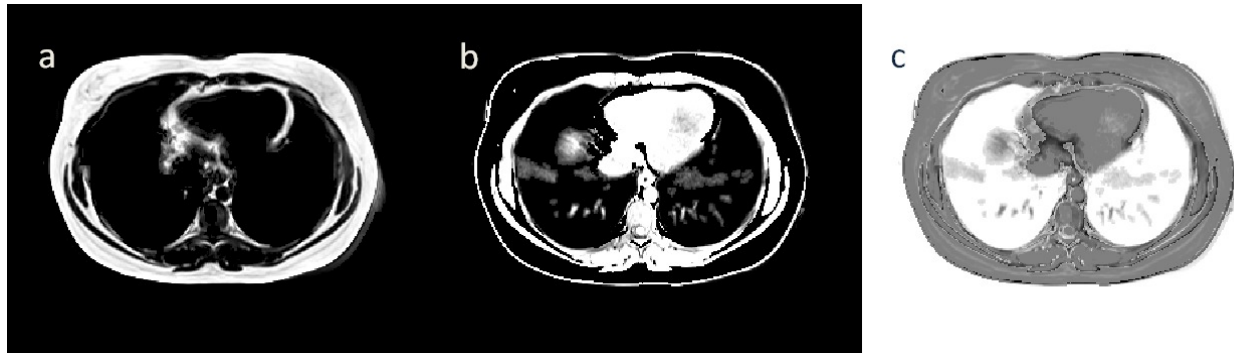
Figure 6. At the slice at the superior-most extent of the diaphragm (subject B), the enhanced and normalized (a) fat-only image, (b) water-only image, and (c) the constructed void "signal" highlighting the lungs.

since the maximum possible value of the sum of the normalized signals ($S_{fat} + S_{water}$) is 2. This approach handles the signal in the lung region on its own right, instead of quantifying a fat fraction (FF) or water fraction (WF) there, either of which could have a high value, in spite of being in a region of low absolute signal intensity. A simple threshold of 1.5 can be used to segment the voids, since a value of 1.0 corresponds merely to a saturated fat-only or water-only signal. To be clear, while we do estimate the FF's and WF's for the entire volumes, as these quantities are useful metrics for intervention studies such as this, they are not so useful for the segmentation algorithm. It should also be noted that our way of estimating FF should be validated with MRS measurements[1].

2.5.4 Segmentation of various tissues

Comparable to existing approaches[6-9], the subsequent segmentation of tissue types is done in stages via morphological and other image processing operations from the enhanced signal foregrounds using the expected distribution, geometric and topological properties of the various tissues. Proceeding along the axial slices, first a body mask is defined slice by slice, by combining the fat and water signals and filling any holes. The annular cross-section of the fat outside the body cavity, the SAT, allows for its segmentation via cut lines and morphological operations, with additional steps added for slices containing the umbilicus. Next, the remainder of the body mask inside the SAT is taken as the body cavity itself, both of which are corrected using the water signal, see Fig. 7. The fat-only signal within the body cavity is classified as internal AT, while the water-only signal inside the body cavity is taken as the internal organs, although technically it is also comprised of connective tissues, some bone tissue and some digestive contents. Larger voids within the thoracic cavity are taken as lung tissue, while smaller voids may be present in the digestive tract. The aggregate internal AT (denoted as VAT+) is then further segmented into intermuscular adipose tissue (IMAT), which is between the muscles that envelope the body cavity; and either as VAT within the abdomen or as thoracic adipose tissue (TAT) above the diaphragm. For abdominal slices this concludes the entire segmentation process, see Fig 9.(a). Note, the average number of abdominal slices is 86 with a slice gap of 0.5 cm, so it is expected that the measured volume and the true volume should be within 5% of each other according to the formula in Ref. [6].

Lastly, the subsequent thoracic segmentation of the heart and its associated adipose tissues[19] is aided by the knowledge of the position and contour of the heart, see Fig. 8. The aorta center is pre-labelled and used as a seed to create the aorta mask, which is expected to be almost circular. The fat within the vicinity of the aorta is classified as peri-aortic adipose tissue (PAAT) using the aorta itself as a seed region. Next, the lungs, aorta and esophagus void are used to frame the heart location, and the main heart organ is defined from the water-only signal. One final issue is dealing with the tissue from other organs, such as the liver and spleen, in the vicinity of the apex of the heart. This is handled by masking the heart downward from the lowest fully thoracic slice, by automatically determining a Bayesian threshold between the higher diaphragm/liver intensities versus the lower heart tissue intensities, and by excluding regions within the convex hulls of each of the lungs and the aorta. The epicardial adipose tissue (EAT) is defined as the fat within the pericardial sac[17], and its segmentation is estimated by dilating the convex hull of the heart. The remaining AT near the heart is deemed to be the paracardial adipose tissue (PAT), which is outside the pericardial sac, see Figure 9(b). In spite of the lack of cardiac gating the pericardial sac is visible in many slices toward the apex of the heart. These slices show good qualitative agreement between the EAT segmentation and its definition as being within the pericardial sac. However, some calibration will be required by comparison with the EAT volume found from cardiac gated medical images.
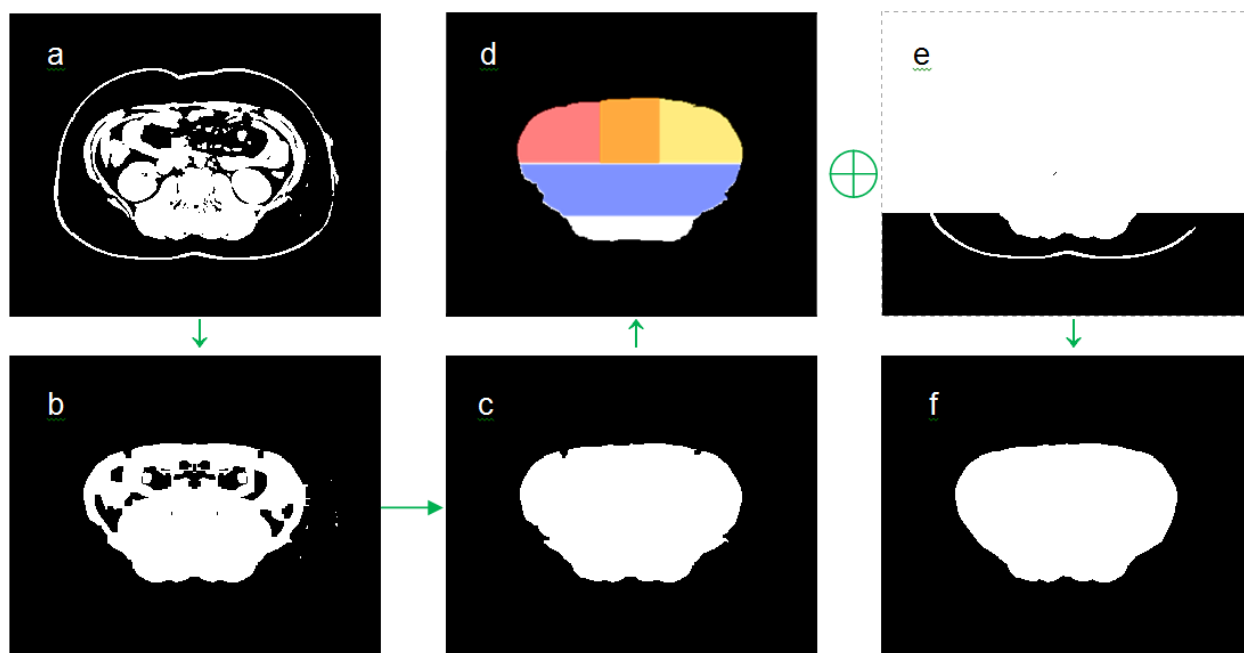
Figure 7. Construction of the body cavity mask: (a) the binary water-only image (derived similarly as Fig. 5.c) is eroded morphologically around the skin (using the body mask) and the remainder is closed to yield (b) which is filled and opened to yield (c) which is again closed to yield (d) which has its edges smoothed by finding the convex hulls of the colored masks and is also masked with (e) a posterior masked and opened form of (a) to finally yield (f) the body cavity mask.
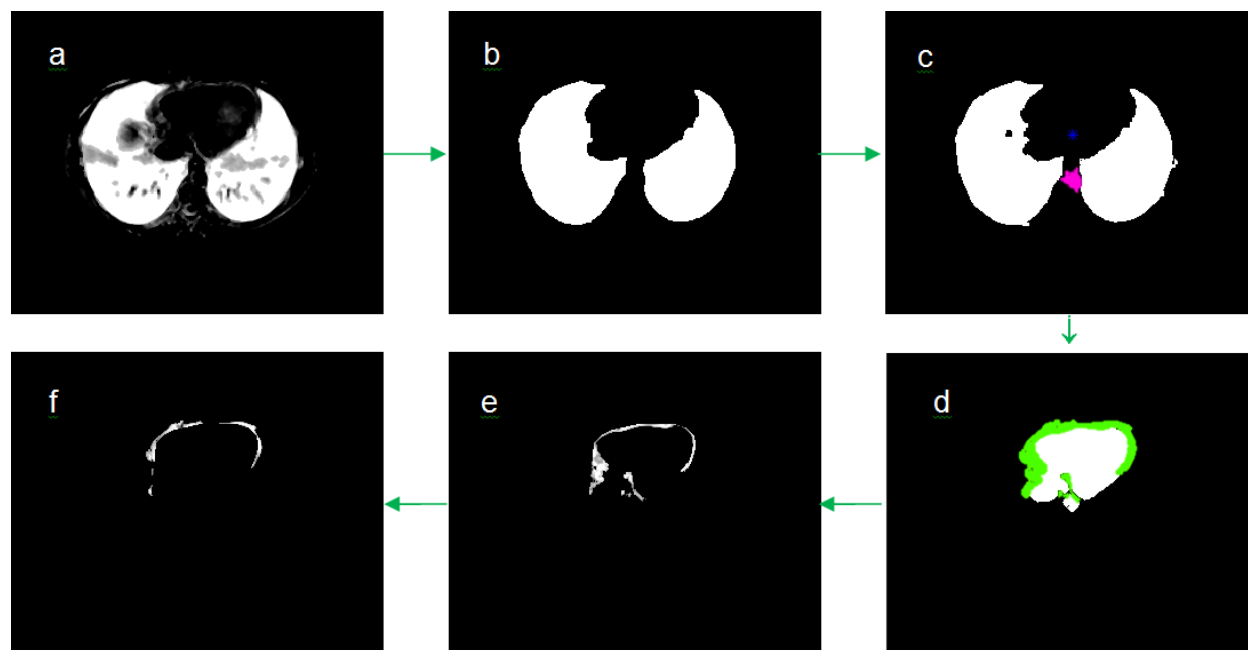

Figure 8. Basic heart and heart fat segmentation: (a) the result for thresholding the void image in Fig. 5.c with intensities > 127 and masking with the body cavity mask, which in turn is automatically thresholded, filled and morphologically opened to yield the preliminary binary mask (b) which is refined around the edges to yield (c) the lung mask (white),which is used along with the aorta + PAAT (pink) to frame the heart via a seed that grows from the centroid (blue asterisk) to yield (d) the preliminary heart mask (white), which later has the esophagus rejected by void detection, and can in turn be used to detect the heart fat by dilation of its convex hull (green), that can be further segmented as (e) the EAT mask and (f) the PAT mask.
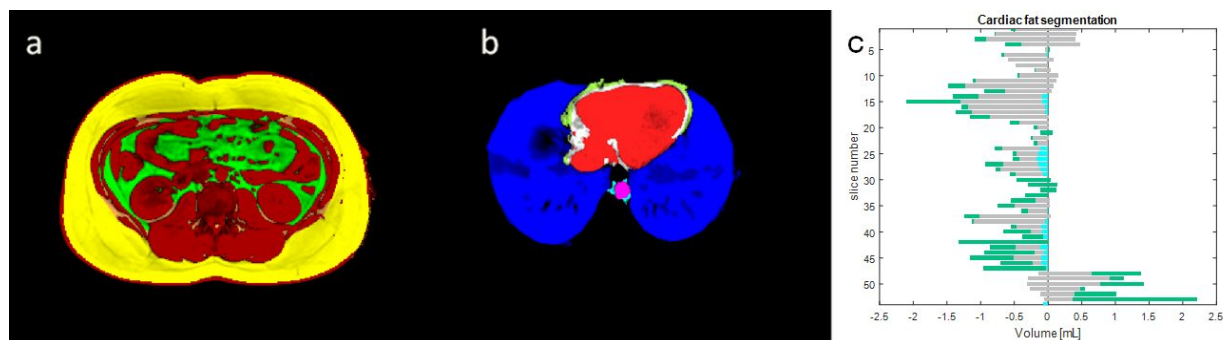
Figure 9. (a) Segmentation of an abdominal slice, where the organs (crimson), voids (dark blue), SAT (yellow), VAT (bright green) and IMAT (beige) are shown; (b) segmentation results of the lungs (bright blue), heart (bright red), EAT (silver), PAT (sea green), aorta (magenta) and PAAT (cyan) are shown; (c) stacked bar graph of the slice by slice changes in the PAAT (cyan), EAT (silver) and PAT (sea green) from pre- to post-intervention scans (subject B).

3. RESULTS

The segmentation results for an abdominal slice and a thoracic slice, as well as the changes in heart fat for subject B are shown in Fig. 9. A summary of the changes observed from the results of our segmentation approach for the four subjects, who took part in our intervention study, is reported in Tab. 1.

Table 1. Results for some of the adipose tissue volume estimations of four subjects.

| Subject	Volume	Abdominal VAT+ [cc]	Peri-aortic AT [cc]	Epicardial AT [cc]	Paracardial AT [cc]
A	pre	4767.33	36.28	111.90	77.09
	post	4776.52	34.97	100.45	66.39
	difference	+9.19	-2.01	-11.44	-10.71
B	pre	3694.97	18.29	117.41	79.21
	post	3490.02	17.36	95.66	78.43
	difference	-204.95	-0.93	-21.74	-0.78
C	pre	3454.66	21.75	79.40	41.35
	post	3449.13	21.82	74.95	38.96
	difference	-5.53	-0.60	-4.45	-2.38
D	pre	5919.30	30.21	139.82	122.40
	post	5889.01	28.66	112.51	108.34
	difference	-30.28	-1.55	-27.31	-14.06
average (standard deviation)	pre	4459.07 (1128.42)	26.63 (8.15)	112.13 (24.94)	80.01 (33.17)
	post	4401.17 (1167.78)	25.70 (7.73)	95.89 (15.66)	73.03 (28.76)
	difference	-57.90 (99.38)	-0.93 (0.63)	-16.23 (10.24)	-6.98 (6.42)
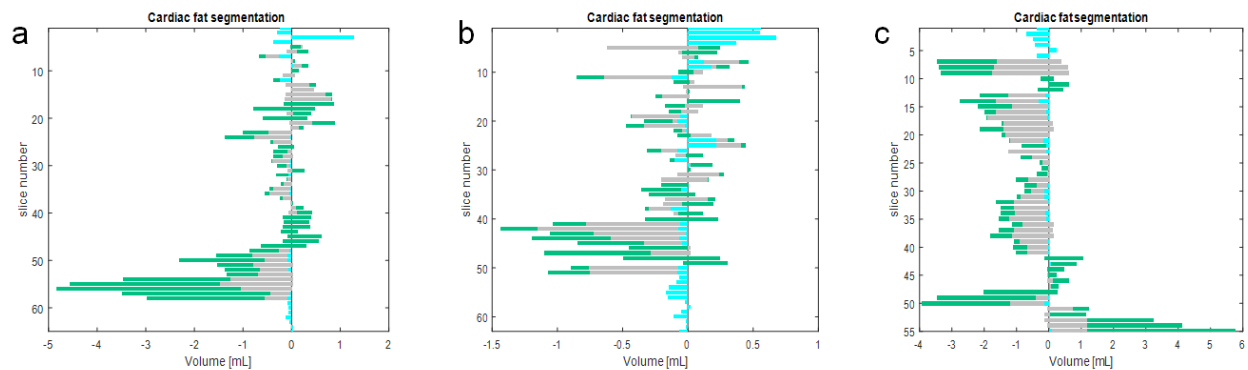
Figure 10. Stacked bar graphs of the slice by slice changes in the PAAT (cyan), EAT (silver) and PAT (sea green) from pre- to post-intervention scans (a) for subject A, (b) for subject C, and (c) for subject D. Note: the EAT bars that cross the 0 line are obscuring the PAAT bar which has an opposite sign for that slice.

Observe how all but one of these adipose tissue volumes decrease after the intervention for all four subjects, with the average EAT decreasing by 14.47%, the average PAT decreasing by 8.72%, and the average PAAT decreases by 3.5% from the initial values, although inter-subject variability indicates that a larger sample size is needed. The stacked bar graph of slice by slice changes in PAAT, EAT and PAT are shown in Fig. 9(c) for subject B and Figure 10 for the other three subjects. The longer bars near the apex of the heart are due partly to the difficulty of the segmentation task in that vicinity, resulting in higher variability for those slices. These bar graphs show consistently slightly smaller cardiac-related AT volumes in the post-intervention scan when compared to the pre-intervention scan, except near the apex of the heart (which has the most inconsistent heart segmentation). A reduction in heart fat depots is associated with better health outcomes[18,19]. Finally, 3D reconstructions of the cardiac-related fat depots are shown in Figure 11.
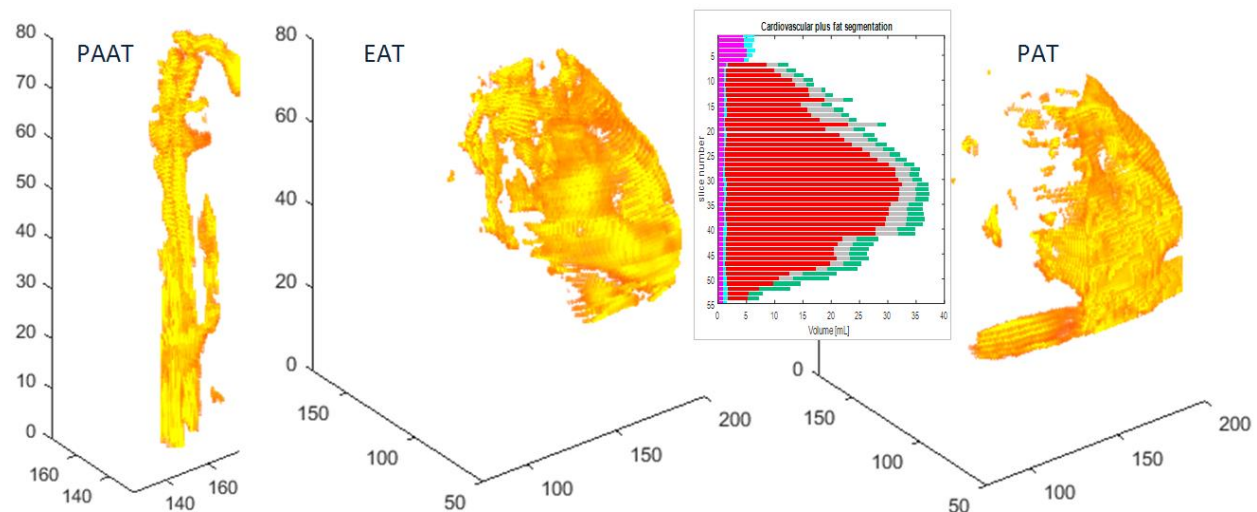

Figure 11. From left to right: PAAT, EAT and PAT 3D volume renderings from pre-intervention data for subject D, where slice number counts up from the diaphragm. The slice by slice volumes displayed as stacked bars going from left to right for the aorta (magenta), PAAT (cyan), heart (red), EAT (silver) and PAT (sea green) tissues are shown in the inset, where slice numbers count down from the most superior slice (near the top of the aorta).

4. CONCLUSION

In this preliminary study with a limited number of subjects, we have shown the application of an in-house MATLAB script to the segmentation of thorax and abdomen volumes acquired by the modified Dixon technique MRI of the body cavity for the purpose of direct assessment of various adipose tissues, which are linked to health outcomes. Specifically, automated segmentation of SAT, VAT, PAAT, and cardiac fat (EAT and PAT) is achieved for comparison and tracking changes in interventional or longitudinal studies. Annotation combined with our rectification technique allows for the slice-by-slice comparison of pre- and post-interventional scans. This work is remarkable because we also applied these data to evaluate fat around the heart, which is usually measured with a cardiac-gated medical image. The advantage of using data from the Dixon-technique MRI is improved contrast between fat and water bearing tissue, while the disadvantage is motion blur around the heart. If a correspondence can be established between the cardiac AT volumes from various methods, this could potentially act as a surrogate for measures obtained from cardiac-gated approaches. Incidentally this segmentation method could also apply to lung imaging via the "void signal", although that is subject to the variability in the breath-hold position. Further work on the segmentation method would involve several refinements, such as fuller annotation of the aorta and esophagus, comparison with existing metrics, and a further segmentation of the thoracic adipose tissue (TAT).

ACKNOWLEDGEMENTS

REFERENCES

[1] Thomas, E. L., Fitzpatrick, J. A., Malik, S. J., Taylor-Robinson, S. D., and Bell, J. D. "Whole body fat: Content and distribution," Progress Nuclear Magn. Res. Spect. 73, 56–80 (2013).

[2] Shen, W.; Wang, Z.; Punyanita, M.; Lei, J.; Sinav, A., Kral, J. G., Imielinska, C., Ross, R. and Heymsfield, S. B., "Adipose tissue quantification by imaging methods: a proposed classification," Obes. Res. 11, 5–16 (2003).

[3] Mitra, S., Fernandez del Valle, M., and Hill, J. E. "The Role of MRI in Understanding the Underlying Mechanisms in Obesity Associated Diseases," BBA-Molecular Basis of Disease, 17 pages, in press (2016).

[4] Kamel, E. G., McNeill, G., Han, T. S., Smith, F. W. Avenell, A. Davidson, L. and Tothill P., "Measurement of abdominal fat by magnetic resonance imaging, dual-energy X-ray absorptiometry and anthropometry in nonobese men and women," Int. J. Obes. Relat. Metab. Disord. 23, 686–692 (1999).

[5] Ross, R.; Léger, L.; Morris, D.; de Guise, J. and Guardo, R. "Quantification of adipose tissue by MRI: relationship with anthropometric variables," J. Appl. Physiol. 72, 787–795 (1992).

[6] Thomas, E. L., Saeed, N., Hajnal, J. V., Brynes, A.; A.P. Goldstone, G. Frost, J.D. Bell, "Magnetic resonance imaging of total body fat," J. Appl. Physiol. 85, 1778–1785 (1998).

[7] Machann, J., Thamer, C., Schnoedt, B., Haap, M., Haring, H.-U., Claussen, C. D., Stumvoll, M., Fritsche, A. and Schick, F., "Standardized Assessment of Whole Body Adipose Tissue Topography by MRI," J. Magn. Reson. Imag. 21, 455–462 (2005).

[8] Kullberg, J., Ahlström, H., Johansson, L., and Frimmel, H. "Automated and reproducible segmentation of visceral and subcutaneous adipose tissue from abdominal MRI," Int. J. Obesity 31, 1806–1817 (2007).

[9] Addeman, B. T., Kutty, S., Perkins, T. G., Soliman, A. S., Wiens, C. N., McCurdy, C. M., Beaton, M. D., Hegele, R.A., and McKenzie, C. A., "Validation of Volumetric and Single-Slice MRI Adipose Analysis Using a Novel Fully Automated Segmentation Method," J. Magn. Reson. Imag. 41, 233–241 (2015).

[10] Bosy-Westphal, A., Kossel, E., Goele, K., Blöcker, T., Lagerpusch, M., Later, W., Heller, M., Glüer C. C. and Müller, M. J. "Association of Pericardial Fat with Liver Fat and Insulin Sensitivity After Diet-Induced Weight Loss in Overweight Women," Obesity 18(11) 2111–2117 (2010).

[11] Dahlqvist Leinhard, O., Johansson, A., Rydell, J., Kihlberg, J., Smedby, Ö, Nyström, F. H., Lundberg, P., and Borga, M. "Quantification of abdominal fat accumulation during hyperalimentation using MRI," Proc. Int. Soc. of Magn. Reson. Med. 10, 206 (2005).

[12] Naclerio F., Rodríguez-Romo, G., Barriopedro-Moro, M. I., Jiménez, A., Alvar, B. A. , and Triplett, N. T. F., "Control of resistance training intensity by the OMNI perceived exertion scale" J Strength Cond Res. 25(7) 1879-88 (2011).

[13] Wile, G. E. and Leyendecker, J. R., "Magnetic resonance imaging of the liver: Sequence optimization and artifacts," Magn. Reson. Imag. Clinics of North America 18(3), 525–547 (2010).

[14] Vogt, F. M., Antoch, G., Hunold, P., Maderwald, S., Ladd, M. E., Debatin, J. F. and Ruehm, S. G., "Parallel acquisition techniques for accelerated volumetric interpolated breath-hold examination magnetic resonance imaging of the upper abdomen: assessment of image quality and lesion conspicuity," J. Magn. Reson. Imag. 21(4) 376–382 (2005).

[15] Hu, H. H., Nayak, K. S., and Goran, M. I. "Assessment of abdominal adipose tissue and organ fat content by magnetic resonance imaging." Obesity Reviews 12(5) e504-e515 (2011).

[16] Otsu, N., "A Threshold Selection Method from Gray-Level Histograms," IEEE Trans. on Systems, Man, and Cybernetics 9 (1) 62–66 (1979).

[17] Kaushik M. and Reddy, Y. M., "Distinction of 'Fat Around the Heart,'" J. Am. Coll. Cardiol 58(15), 1640 (2011).

[18] Guzzardi, M. A. and Iozzo, P., "Fatty heart, cardiac damage, and inflammation," Rev. Diabetic Studies: RDS 8(3), 403 (2011).

[19] Shimabukuro, M., Kozuka, C., Taira, S., Yabiku, K., Dagvasumberel, M., Ishida, M., Matsumoto, S., Yagi, S., Fukuda, D., Yamakawa, K., Higa, M., Soeki, T., Yoshida, H., Masuzaki, H. and Sata, M. "Ectopic fat deposition and global cardiometabolic risk: new paradigm in cardiovascular medicine," J. Med. Invest. 60(1-2), 1–14 (2013).